Interpreting Convolutional Neural Networks for Device-Free Wi-Fi Fingerprinting Indoor Localization via Information Visualization

KEVIN M. CHEN [ID][1]**, RONALD Y. CHANG** [ID][1]**, (Member, IEEE), AND SHING-JIUAN LIU** [ID][2]

[1]Research Center for Information Technology Innovation, Academia Sinica, Taipei 11529, Taiwan
[2]Department of Electrical and Computer Engineering, University of California at Davis, Davis, CA 95616, USA

Corresponding author: Ronald Y. Chang (rchang@citi.sinica.edu.tw)

ABSTRACT In this paper, we propose a convolutional neural network (CNN) model for device-free fingerprinting indoor localization based on Wi-Fi channel state information (CSI). Besides, we develop an interpretation framework to understand the representations learned by the model. By quantifying and visualizing CNN in comparison with the fully-connected feedforward deep neural network (DNN) (or multilayer perceptron), we observe that each model can automatically identify location-specific patterns, which are however different across models and are linked to the respective performance of each model. Furthermore, we quantify how features, relevant or otherwise, as deemed by the adopted quantifying metrics (i.e., relevance scores, calculated by relevance propagation techniques), determine or affect the performance results. Interpretation of learning models for wireless applications is challenging due to the lack of human sensory intuition and reference. The results presented in this paper provide visually perceivable evidence and plausible explanations for the performance advantages of CNN in this important application.

INDEX TERMS Wireless indoor localization, convolutional neural networks (CNN), fingerprinting, Wi-Fi, channel state information (CSI), Internet of Things (IoT), visualization.

I. INTRODUCTION

Wireless indoor localization is a key enabling technology for the Internet of Things (IoT) [1]. Precise location information is crucial for many futuristic IoT applications, such as smart cities and smart homes [2], disaster management and drone-assisted rescue services [3], [4], health care and assisted living [5], vehicle-to-everything (V2X) services [6]–[8], etc. Fingerprinting-based techniques with Wi-Fi measurements are a widely adopted solution for indoor localization. Fingerprinting refers to building an offline database ("fingerprints") of wireless signal measurements and then matching the online measurements with the offline database to determine the location of the target. A commonly used measurement parameter is the received signal strength (RSS). However, for orthogonal frequency-division multiplexing (OFDM)-based Wi-Fi radios, channel state information (CSI) carries advantageous potential as the measurement parameter, as it provides fine-grained link information in the granularity

of a single OFDM subcarrier [9]. From a device perspective, indoor localization techniques can be classified as device-based or device-free [10]. While the device-based approach generally provides higher accuracy, the device-free approach serves broader general-purpose use cases (especially in the IoT era) and has additional benefits such as lower cost and higher privacy, since no tracking device needs to be equipped by the target.

Deep learning-based approaches have been studied for fingerprinting-based indoor localization (both device-based and device-free) due to their recent advances and successes in various domain applications. Wang *et al.* [11] proposed a deep learning-based framework for device-based indoor localization, which includes a greedy learning algorithm to train the weights of a multilayer network in the offline training phase and a probabilistic method to estimate the location based on CSI measurements in the online testing phase. BelMannoubi and Touati [12] proposed a stacked autoencoder-based (SAE) model, where two stacked autoencoders are trained in an unsupervised manner to recognize RSS signals for device-based Wi-Fi indoor localization. Chen *et al.* [13]

The associate editor coordinating the review of this manuscript and approving it for publication was Maurice J. Khabbaz [ID].

K. M. Chen *et al.*: Interpreting CNNs for Device-Free Wi-Fi Fingerprinting Indoor Localization via Information Visualization

IEEE Access

proposed a local feature-based deep long short-term memory (LF-DLSTM) approach for Wi-Fi indoor localization with RSS, which consists of a local feature extractor that extracts robust local features and the DLSTM model that learns high-level representations from the extracted features. Liu *et al.* [14] proposed a deep neural network (DNN)-based classification model for device-free indoor localization. CSI pre-processing and data augmentation were introduced into the proposed DNN model to improve the localization performance. Wang *et al.* [15] proposed a deep convolutional neural network (DCNN)-based classification model for device-based indoor localization. The phase information of the CSI measurements is extracted to estimate the angle of arrival (AoA), which forms an image-type input for DCNN. The AoA images are used to train the DCNN model for location estimation. Hsieh *et al.* [16] compared different deep learning models with different measured Wi-Fi parameters for fingerprinting-based device-free indoor localization, and concluded that convolutional neural network (CNN)-based model with CSI achieves the best performance.

While a deep learning model performs impressively well in practice, its lack of transparency, resulted from the abstract and nonlinear processes through multiple layers without human intervention, restricts its interpretability. This issue has received increasing attention. Research that aims to open the black box of multilayer neural networks has been conducted, mostly in the domain of image classification. Kuo [17] proposed a mathematical model to explain why nonlinear activations in CNNs are essential and what advantages the multilayer cascade structure of CNNs offers. Tishby and Zaslavsky [18] analyzed DNN via the theoretical framework of the information bottleneck (IB) principle and suggested that any DNN can be quantified by the mutual information and the optimal information theoretic limits of DNN can be computed. Visualization techniques proved to be a handy tool to understand the learning process of the multilayer neural networks [19].

Several approaches for network visualization have been proposed, e.g., the deconvolution method [20], [21] and the layer-wise relevance propagation (LRP) method [22], [23], both essentially mapping the network output decisions to the pixel space for interpretation and visualization. The deconvolution method [20] visualizes the activities within the model and the visualization results are used to demonstrate the learning process of the model as well as for model improvement. Balu *et al.* [21] proposed the forward-backward approach for visualizing the information flow in DNNs based on the approach in [20], with reduced computations since it only needs matrix adjoints and (element-wise) nonlinearities for each convolutional layer. The LRP method [22], [23], and its cousin, the deep Taylor decomposition method [24], decompose the output decision and backpropagate neuron-wise contributions from the output to the input layer. It was shown [25] that the LRP method provides a better pixel-wise visual interpretation of model decisions than the deconvolution method.

In this paper, we aim at two objectives: i) proposing a CNN model for device-free Wi-Fi fingerprinting indoor localization, and ii) inspired by similar work in image classification, interpreting the CNN prediction in device-free Wi-Fi fingerprinting indoor localization by adapting and explicitly formulating the LRP method for the CNN architecture. To the best of our knowledge, this is the first work to provide visually perceivable evidence and plausible explanations for CNN in this specific application. Our main results are:

1) The CNN model achieves superior precision, recall, and F1-score performances as compared to the k-nearest neighbor (k-NN), support vector machine (SVM), and the fully-connected feedforward DNN model in two real-world scenarios, and has much fewer trainable parameters as compared to DNN.
2) CNN observes more clear and explicit location-specific patterns, as revealed by the greater polarization in the distribution of relevance scores (calculated by LRP), as compared to DNN. This suggests that CNN can focus on a smaller subset of relevant, discriminative features, which may help explain the better performance of CNN.
3) For both CNN and DNN, a small subset of features with the highest relevance scores dominates the model prediction.

The rest of the paper is organized as follows. Section II describes the indoor localization problem and the experimental settings. Section III describes the proposed CNN model for localization. Section IV introduces the method for interpreting CNN prediction via LRP. Section V presents the performance and interpretation results and discussion. Finally, Section VI concludes the paper.

II. PROBLEM DESCRIPTION AND EXPERIMENTAL SETTINGS

We consider the fingerprinting-based device-free Wi-Fi indoor localization problem. The problem is to locate a person in an indoor environment as one of the prespecified M target locations. A single fixed-location Wi-Fi transmitter and a single fixed-location receiver are deployed in the indoor environment. No tracking device is attached to the target person (i.e., device-free). The receiver receives wireless signals from the transmitter after reflection, diffraction, absorption, scattering, etc. of the wireless signals off the target, and collects the channel state information (CSI). CSI provides fine-grained link information in the granularity of a single OFDM subcarrier as compared to the received signal strength (RSS) which provides coarse-grained information of the overall received signal power [9]. The CSI data are collected in both offline training and online testing phases, and the fingerprinting technique is used to locate the target person by matching the online testing data with the offline database.

We conduct two real-world experiments at the Research Center for Information Technology Innovation, Academia Sinica, as described below.
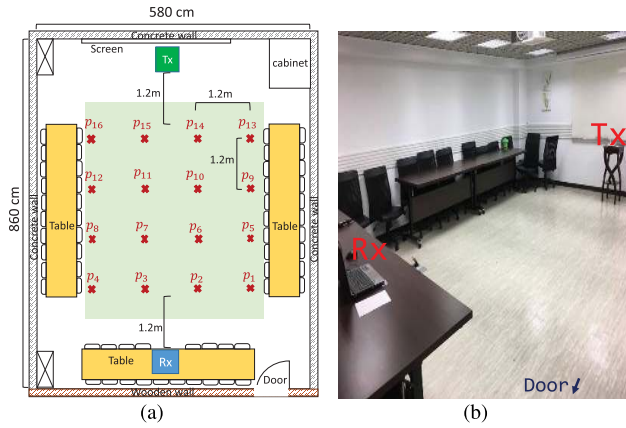
IEEE Access

K. M. Chen *et al.*: Interpreting CNNs for Device-Free Wi-Fi Fingerprinting Indoor Localization via Information Visualization

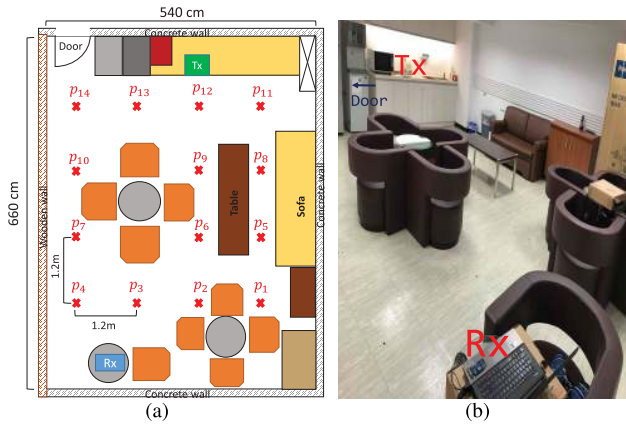**FIGURE 1.** Scenario 1. (a) Floor plan. (b) Photograph.

FIGURE 2. Scenario 2. (a) Floor plan. (b) Photograph.

Scenario 1: The experimental scenario here is a conference room with dimensions 5.8×8.6 m^2, as depicted in Fig. 1. There are $M = 16$ target locations, labeled by $p_1, p_2, \ldots, p_{16}$, which are 1.2 m apart between two nearest locations. One Zyxel NBG-419N Wi-Fi access point (AP) as the transmitter (Tx) and one ASUS laptop with Intel Wi-Fi Link 5300 802.11n MIMO-OFDM radios [26] as the receiver (Rx) are placed at fixed locations with heights 88 cm and 82 cm, respectively. In the offline training phase, the training data are collected in two consecutive days at four different times each day (morning, noon, afternoon, and evening). 100 CSI samples were collected at each time; hence, 400 CSI samples were collected for each location (6400 for all locations). In the online testing phase, a similar procedure is performed in two different times (morning and afternoon), which results in 200 CSI samples for each location (3200 for all locations). Each CSI sample is a W-dimensional vector, where $W = 120$ as specified by the number of OFDM subcarriers (i.e., 30) multiplied by the 2×2 transmit-receive antenna pairs. Each element of the CSI sample is termed a *CSI channel*, or simply *channel*, in this paper.

Scenario 2: The experimental scenario here is a lounge with dimensions 5.4×6.6 m^2, as depicted in Fig. 2. There are $M = 14$ target locations, labeled by $p_1, p_2, \ldots, p_{14}$, which are 1.2 m apart between two nearest locations. The Wi-Fi transmitter and receiver are similarly deployed as in Scenario 1, but at heights 76 cm and 69 cm, respectively.

In the offline training phase, the training data are collected in two consecutive days at six different times of two hours apart each day. 128 CSI samples were collected at each time; hence, 768 CSI samples were collected for each location (10752 for all locations). In the online testing phase, a similar procedure is performed in two different times in the same day, which results in 184 CSI samples for each location (2576 for all locations).

Note that the room dimensions and the distances between two nearest training points in both experimental scenarios are comparable to those considered in [27]–[29]. The two scenarios exemplify practical indoor environments with different room layouts and indoor objects.

III. CNN-BASED MODEL FOR LOCALIZATION

As depicted in Fig. 3, the proposed CNN model is composed of an input layer, $L = 3$ convolutional layers, and an output layer. The input layer accepts the $W = 120$ dimensional CSI sample vector, denoted as $\mathbf{x} = [x_1, x_2, \ldots, x_W]^T$. The first convolutional layer (denoted by Conv-1) filters the input CSI $\mathbf{x}$ with $K^{(1)} = 32$ kernels (or filters) of size $F^{(1)} \times 1 = 5 \times 1$, and stride $S = 1$. This is illustrated in Fig. 3 as $32@5 \times 1$ filters. The output volume of Conv-1 is of dimensions $W^{(1)} \times H^{(1)}$, where $W^{(1)} = (W - F^{(1)})/S + 1 = 116$ and $H^{(1)} = K^{(1)} = 32$. The output of neuron i in the hth slice of Conv-1 (resulting from the hth kernel of Conv-1) is described as

$$a_{h,i}^{(1)} = ReLU\left(\sum_{f=0}^{F^{(1)}-1} x_j \times w_{h,1,j,i}^{(1)} + b_h^{(1)}\right), \quad j = i+f \quad (1)$$

where $w_{h,d,j,i}^{(l)}$ denotes the weight connecting neuron j in the hth slice of the lth convolutional layer (denoted by Conv-l) and neuron i in the dth slice of the previous layer (here, $l = 1$ and $d = 1$ since the previous layer is the input layer), $b_h^{(l)}$ denotes the bias of the hth kernel of Conv-l (here, $l = 1$), and $ReLU(\cdot)$ is the nonlinear activation function.

Subsequent convolutional layer operations can be modeled similarly. Conv-l ($l = 2, \ldots, L$) filters the $W^{(l-1)} \times H^{(l-1)}$ output (or feature map) of Conv-$(l-1)$ with $K^{(l)} = 32$ kernels of size $F^{(l)} \times D^{(l)}$, where $F^{(l)} = 5$ and $D^{(l)} = H^{(l-1)}$, and stride $S = 1$. The output volume of Conv-l ($l = 2, \ldots, L$) is of dimensions $W^{(l)} \times H^{(l)}$, where $W^{(l)} = (W^{(l-1)} - F^{(l)})/S + 1$ and $H^{(l)} = K^{(l)}$. Consider $l = 2$ as an example. Conv-2 filters the $W^{(1)} \times H^{(1)} = 116 \times 32$ output of Conv-1 with $K^{(2)} = 32$ kernels of size $F^{(2)} \times D^{(2)} = 5 \times 32$, resulting in an output of dimensions $W^{(2)} \times H^{(2)} = \left[(W^{(1)} - F^{(2)})/S + 1\right] \times K^{(2)} = 112 \times 32$. The filter and output dimensions for Conv-2 are illustrated in Fig. 3. Likewise, the filter and output dimensions for Conv-3 can be calculated and are also illustrated in Fig. 3. The output of neuron i in the hth slice of Conv-l (resulting from the hth kernel of Conv-l) for $l = 2, \ldots, L$ is described as

$$a_{h,i}^{(l)} = ReLU\left(\sum_{d=1}^{D^{(l)}} \sum_{f=0}^{F^{(l)}-1} a_{d,j}^{(l-1)} \times w_{h,d,j,i}^{(l)} + b_h^{(l)}\right), \quad j = i+f.$$

$$(2)$$

K. M. Chen *et al.*: Interpreting CNNs for Device-Free Wi-Fi Fingerprinting Indoor Localization via Information Visualization
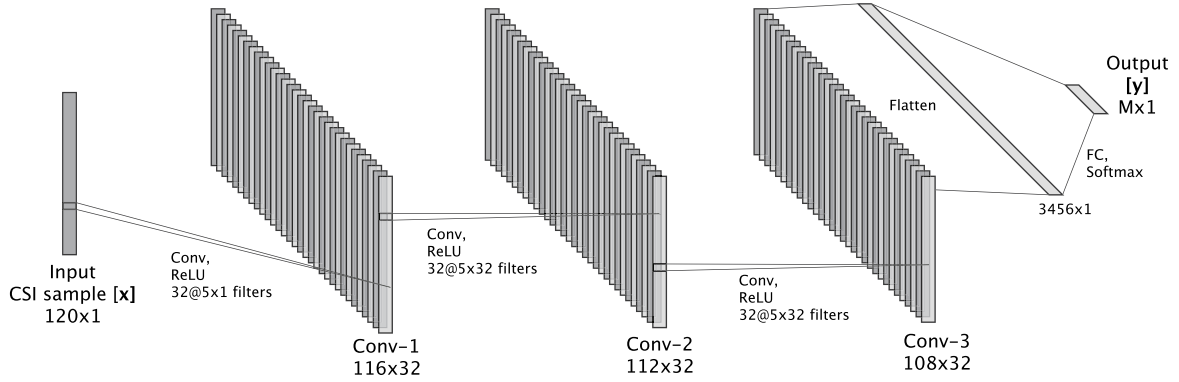
IEEE *Access*

FIGURE 3. Architecture overview of the proposed CNN model for device-free fingerprinting indoor localization based on Wi-Fi CSI. The model accepts CSI sample with 120 channels as its input. Each convolutional layer is performed with 32 filters, a stride of one, and ReLU nonlinear activation. The softmax fully-connected (FC) layer produces the model output y.

After the operations of all convolutional layers, the output of Conv-L is flattened into a 1D feature vector $\mathbf{a}^{(L)} = [a_1^{(L)}, a_2^{(L)}, \ldots, a_K^{(L)}]$, where $K = W^{(L)} \times H^{(L)}$. In our model with $L = 3$ convolutional layers, $K = W^{(3)} \times H^{(3)} = 108 \times 32 = 3456$, as illustrated in Fig. 3. The output layer is a fully-connected layer that accepts $\mathbf{a}^{(L)}$ as its input and produces a softmax output denoted by $\mathbf{y} = [y_1, y_2, \ldots, y_M]$. The model prediction is location p_m, where y_m is the maximum value in $\mathbf{y}$.

Note that downsampling and regularization techniques such as pooling and dropout [30] are not incorporated in the proposed CNN model, since the original input CSI data are of a relatively small dimension already, as compared to images. In fact, it is numerically verified in our extensive simulations that incorporating pooling layer(s) and/or dropout results in degraded performance.

IV. METHODS FOR INTERPRETING CNN PREDICTION
Layer-wise relevance propagation (LRP) [22], [23] was developed to quantify the contribution of the input data to a specific output prediction. Here, we adapt LRP to the CNN architecture. LRP first decomposes the softmax value of the model prediction, y_m, into *relevance scores* of the neurons in the previous layer and backpropagates the scores toward the input layer to obtain the relevance score of CSI channel i in the input layer, denoted by R_i. The conservation principle [23] constrains the summation of the relevance scores of each layer to be equal to y_m. The relevance score of neuron i of the 1D feature vector of Conv-L is given by

$$R_i^{(L)} = \frac{a_i^{(L)} \left(w_{m,i}^{(L+1)}\right)^+}{\sum_j a_j^{(L)} \left(w_{m,j}^{(L+1)}\right)^+} y_m, \quad i = 1, \ldots, K \quad (3)$$

where $w_{m,i}^{(L+1)}$ is the weight connecting neuron m in the output layer and neuron i of the 1D feature vector of Conv-L, and $(x)^+ = \max(0, x)$. By backward calculations, the relevance scores of neuron i in the dth slice of Conv-l ($l = 1, 2, \ldots, L-1$), and of CSI channel i in the input layer, are given

respectively by

$$R_{d,i}^{(l)} = \sum_h \sum_k \frac{a_{d,i}^{(l)} \left(w_{h,d,k,i}^{(l+1)}\right)^+}{\sum_{d=1}^{D^{(l)}} \sum_{f=0}^{F^{(l+1)}-1} a_{d,j}^{(l)} \left(w_{h,d,j,i}^{(l+1)}\right)^+} R_{h,k}^{(l+1)},$$
$$j = i + f, \quad (4)$$

$$R_i = \sum_h \sum_k \frac{x_i \left(w_{h,1,k,i}^{(1)}\right)^+}{\sum_{f=0}^{F^{(1)}-1} x_j \left(w_{h,1,j,i}^{(1)}\right)^+} R_{h,k}^{(1)}, \quad j = i + f. \quad (5)$$

Note that when $l = L - 1$, $R_{h,k}^{(L)}$ in the right-hand-side of (4) is equal to $R_i^{(L)}$ in (3) with $i = (h - 1)W^{(L)} + k$, by index mapping from 2D to 1D. Finally, R_i in (5), which is always positive-valued, is normalized to the interval $[0, 1]$, i.e.,

$$R_i' = \frac{R_i}{\max_{j=1,\ldots,W} R_j}. \quad (6)$$

Values of R_i' close to one suggest that CSI channel i provides positive evidence supporting the model prediction, and values of R_i' close to zero suggest that CSI channel i provides negligible evidence for the model prediction. The computational flow of LRP is illustrated in Fig. 4.

To examine how each CSI channel contributes to the model prediction, we propose the *channel nullification* procedure. The procedure is to sequentially nullify each CSI channel in the ascending or descending order of the relevance scores of the CSI channels. 'Descending' means CSI channels with the highest relevance scores are nullified first, and 'ascending' means CSI channels with the lowest relevance scores are nullified first. When a channel is nullified, the value of that channel is set to zero.

V. RESULTS AND DISCUSSION
The performance of the CNN and the interpretation of its learning results are presented in this section. Statistical performance measures of precision, recall, and F1-score are considered. The precision and recall quantify the percentages of correct classification for each predicted class and true class, respectively, and the F1-score is the harmonic mean of precision and recall.

IEEE *Access*

K. M. Chen *et al.*: Interpreting CNNs for Device-Free Wi-Fi Fingerprinting Indoor Localization via Information Visualization

TABLE 1. Scenario 1: Location-Wise and Average Statistical Performance of *k*-NN, SVM, DNN, and CNN.

Measure	Scheme	p_1	p_2	p_3	p_4	p_5	p_6	p_7	p_8	p_9	p_{10}	p_{11}	p_{12}	p_{13}	p_{14}	p_{15}	p_{16}	Avg.
Precision	*k*-NN	0.83	1.00	0.51	0.90	0.88	0.98	1.00	0.93	0.36	0.75	0.96	0.97	0.40	0.99	1.00	0.88	0.83
	SVM	0.65	1.00	0.52	1.00	1.00	1.00	0.98	0.99	0.62	0.74	0.98	1.00	0.54	1.00	1.00	0.89	0.87
	DNN	0.80	0.93	0.43	0.82	0.92	0.89	0.98	0.57	0.90	0.89	0.98	0.78	0.84	1.00	0.99	0.93	0.85
	CNN	0.79	1.00	0.87	0.69	0.99	1.00	0.93	0.94	0.74	0.75	0.98	0.99	0.95	1.00	1.00	0.90	0.91
Recall	*k*-NN	0.23	0.53	0.93	0.48	0.18	1.00	1.00	0.93	0.99	1.00	0.78	0.74	0.64	0.57	0.61	1.00	0.73
	SVM	0.41	0.80	0.97	0.69	0.07	1.00	1.00	0.86	0.94	0.96	1.00	1.00	0.92	0.51	0.89	1.00	0.81
	DNN	0.41	0.92	0.47	0.59	0.89	1.00	1.00	0.96	0.87	0.97	0.98	0.91	0.93	0.50	1.00	1.00	0.84
	CNN	0.95	1.00	0.65	0.66	0.78	1.00	1.00	0.93	1.00	1.00	1.00	0.99	0.92	0.50	0.98	1.00	0.90
F1-score	*k*-NN	0.35	0.69	0.66	0.63	0.30	0.99	1.00	0.93	0.53	0.86	0.86	0.84	0.49	0.73	0.76	0.94	0.72
	SVM	0.50	0.89	0.68	0.82	0.13	1.00	0.99	0.93	0.74	0.84	0.99	1.00	0.68	0.68	0.94	0.94	0.80
	DNN	0.54	0.93	0.44	0.69	0.90	0.94	0.99	0.72	0.89	0.93	0.98	0.84	0.88	0.67	1.00	0.96	0.83
	CNN	0.86	1.00	0.74	0.67	0.87	1.00	0.96	0.94	0.85	0.86	0.99	0.99	0.93	0.67	0.99	0.95	0.89

TABLE 2. Scenario 2: Location-Wise and average statistical performance of *k*-NN, SVM, DNN, and CNN.

Measure	Scheme	p_1	p_2	p_3	p_4	p_5	p_6	p_7	p_8	p_9	p_{10}	p_{11}	p_{12}	p_{13}	p_{14}	Avg.
Precision	*k*-NN	0.18	0.21	1.00	0.00	0.36	0.60	0.80	0.25	0.24	0.77	0.32	0.17	1.00	0.11	0.43
	SVM	0.91	0.42	1.00	0.98	0.93	0.47	0.99	0.61	0.61	0.73	0.76	0.21	1.00	1.00	0.76
	DNN	0.87	0.30	1.00	1.00	0.95	0.39	0.59	0.97	0.48	0.92	0.66	0.58	1.00	0.98	0.76
	CNN	0.94	0.94	0.99	0.23	0.99	0.49	1.00	0.92	1.00	0.97	0.72	0.79	1.00	0.97	0.85
Recall	*k*-NN	0.11	0.30	0.83	0.00	0.26	0.53	0.49	0.48	0.53	0.57	0.16	0.51	0.20	0.03	0.36
	SVM	0.65	0.81	0.94	0.43	0.65	0.85	0.65	0.65	0.65	0.65	0.39	0.52	0.30	0.45	0.61
	DNN	0.65	0.99	0.89	0.53	0.65	0.69	0.65	0.64	0.65	0.65	0.32	0.59	0.29	0.47	0.62
	CNN	0.65	0.65	0.85	1.00	0.65	0.67	0.65	0.65	0.61	0.65	0.65	0.65	0.39	0.60	0.67
F1-score	*k*-NN	0.13	0.25	0.90	0.00	0.30	0.57	0.61	0.33	0.33	0.65	0.22	0.25	0.33	0.04	0.35
	SVM	0.76	0.56	0.97	0.60	0.76	0.60	0.79	0.63	0.63	0.69	0.51	0.30	0.46	0.62	0.63
	DNN	0.75	0.46	0.94	0.69	0.77	0.50	0.62	0.77	0.56	0.76	0.43	0.59	0.45	0.64	0.64
	CNN	0.77	0.77	0.91	0.37	0.78	0.56	0.79	0.76	0.76	0.78	0.68	0.72	0.56	0.74	0.71

A. PERFORMANCE

The proposed CNN achieves superior performance as compared to *k*-NN, SVM, and DNN, and has fewer trainable parameters as compared to DNN. A proper value of k, i.e., $k = 5$, is adopted for the k-NN, as other typical values all produce similar performance. Radial basis function (RBF) kernel and the one-against-one approach for multi-class classification [31] is adopted for the SVM model. The DNN model is a fully-connected feedforward network (aka the multilayer perceptron) with three fully-connected hidden layers (denoted by FC-1, FC-2, and FC-3) of 300, 280, and 260 neurons, respectively, and one fully-connected output layer (denoted by FC-output). The numbers of neurons in the hidden layers of DNN are determined by cross-validating the model performance with different configurations, and sufficient numbers of neurons are chosen. Further increasing the numbers of neurons leads to saturating performance according to our extensive experiments. Both CNN and DNN models are trained with the same dataset as described in Section II, by using TensorFlow with the Adam optimizer [32] and cross-entropy loss function.

Table 1 and Table 2 present the statistical performance of the proposed CNN in comparison with k-NN, SVM, and DNN in Scenario 1 and Scenario 2, respectively. As can be seen, CNN generally yields higher precision, recall, and F1-score performances, both location-wise and on average, in both scenarios. Also, all schemes achieve deteriorated performance in Scenario 2, because, as will be visually presented later, the CSI data are more noisy due to more obstructions in the indoor environment in Scenario 2.

Table 3 summarizes the number of trainable parameters (weights and biases) for CNN and DNN. The fully-connected layer structure in DNN results in a large number of weights
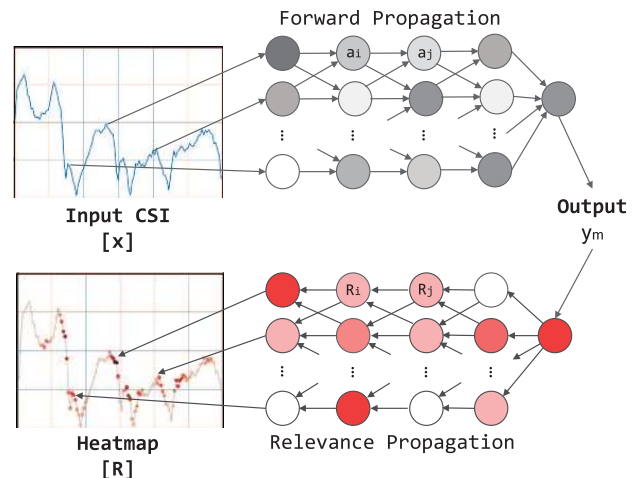

FIGURE 4. The computational flow of LRP. The prediction is obtained by forward propagating CSI sample vector x. The relevance scores in the input layer are obtained by decomposing the softmax value of the prediction into relevance scores of the neurons in the previous layer and then backpropagating the scores toward the input, which are visualized as a heatmap at the input.

to train. In contrast, the convolutional layers in CNN employ shared weights of kernels, thereby dramatically reducing the number of parameters to train. For example, the input to Conv-1 of CNN has $F^{(1)} \times K^{(1)} = 5 \times 32 = 160$ weights and $K^{(1)} = 32$ biases, whereas the input to FC-1 of DNN has $120 \times 300 = 36000$ weights and 300 biases. Overall, the total number of trainable parameters for CNN is only 33% of that of DNN.

B. ANALYSIS OF MODEL PREDICTION

CNN observes more explicit location-specific patterns, as revealed by greater polarization in the distribution of relevance scores, as compared to DNN. A model makes

K. M. Chen *et al.*: Interpreting CNNs for Device-Free Wi-Fi Fingerprinting Indoor Localization via Information Visualization

IEEE *Access*

TABLE 3. The number of trainable parameters (weights and biases) of CNN and DNN.

DNN		CNN	
Layer	Parameters	Layer	Parameters
FC-1	36,300	Conv-1	192
FC-2	84,280	Conv-2	5,152
FC-3	73,060	Conv-3	5,152
FC-output	4,176	FC-output	55,312
Total	197,816	Total	65,808

(a)

(b)
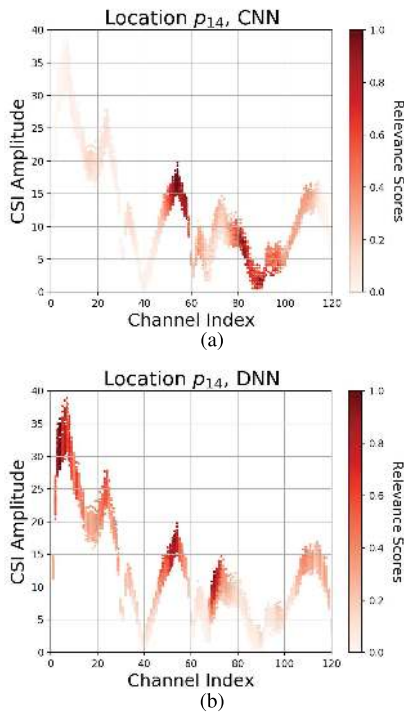
FIGURE 5. Scenario 1: Heatmaps of relevance scores $R'_i, i = 1, \ldots, 120$ superimposed on all testing samples predicted as (a) location p_{14} for CNN and (b) location p_{14} for DNN. The location corresponding to the best precision performance for each model (1.00 for both CNN and DNN) is chosen.

(a)

(b)

FIGURE 6. Scenario 1: Heatmaps of relevance scores $R'_i, i = 1, \ldots, 120$ superimposed on all testing samples predicted as (a) location p_4 for CNN and (b) location p_3 for DNN. The location corresponding to the worst precision performance for each model (0.69 for CNN and 0.43 for DNN) is chosen.

(a)

(b)

FIGURE 7. Scenario 2: Heatmaps of relevance scores $R'_i, i = 1, \ldots, 120$ superimposed on all testing samples predicted as (a) location p_{13} for CNN and (b) location p_{13} for DNN. The location corresponding to the best precision performance for each model (1.00 for both CNN and DNN) is chosen.

classification decision based on the patterns it learned about each location. The patterns are visual representations of how each location looks like in view of a model. Intuitively, more clear and explicit location-specific patterns will lead to better classification performance. The results for the two scenarios are discussed as follows. For Scenario 1, Fig. 5 shows the heatmaps of relevance scores superimposed on all testing samples predicted as location p_{14} for CNN and DNN, and Fig. 6 shows the heatmaps of relevance scores superimposed on all testing samples predicted as location p_4 for CNN and p_3 for DNN. The locations corresponding to the best and worst precision performance for each model are shown in Fig. 5 and Fig. 6, respectively. For Scenario 2, Fig. 7 and Fig. 8 plot the results, where the locations corresponding to the best and worst precision performance for each model are shown here as well. The relevance scores for DNN are calculated using a similar technique as described in Section IV.

It is observed from Figs. 5–8 that, for the same location, CNN and DNN yield different distributions of relevance scores. Specifically, CNN yields more concentrated, polarized-valued rele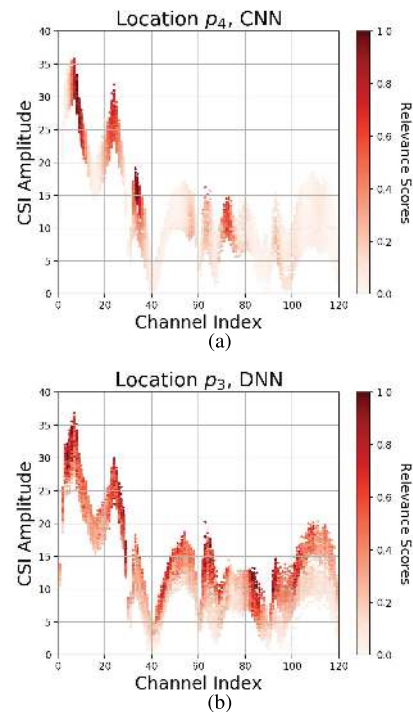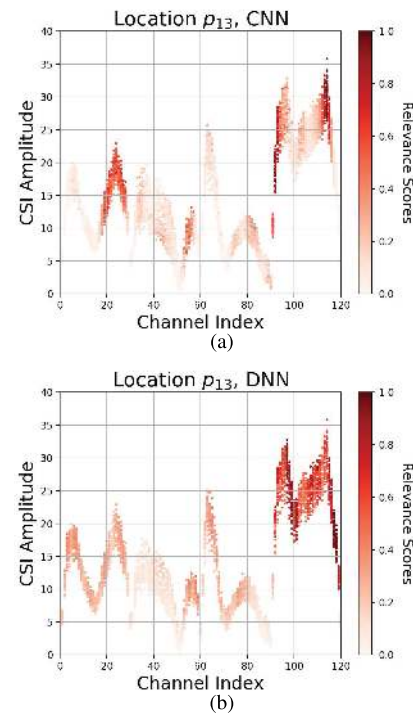vance scores over a smaller number of CSI channels, while DNN yields more moderate-valued relevance scores spread over a larger number of CSI channels.

IEEE *Access*

K. M. Chen *et al.*: Interpreting CNNs for Device-Free Wi-Fi Fingerprinting Indoor Localization via Information Visualization

TABLE 4. Scenario 1: Coefficient of variation of relevance scores, across CSI channels and averaged over all CSI samples (CV (channels)), and across CSI samples and averaged over all CSI channels (CV (samples)).

Measure	Scheme	p_1	p_2	p_3	p_4	p_5	p_6	p_7	p_8	p_9	p_{10}	p_{11}	p_{12}	p_{13}	p_{14}	p_{15}	p_{16}	Avg.
CV (channels)	DNN	0.67	0.68	0.64	0.67	0.55	0.66	0.79	0.81	0.62	0.64	0.67	0.61	0.61	0.82	0.63	0.74	0.68
	CNN	0.93	1.13	1.20	1.28	0.95	0.99	0.85	0.87	1.03	0.88	0.86	1.14	1.07	0.99	0.99	1.02	1.01
CV (samples)	DNN	0.35	0.34	0.45	0.36	0.24	0.27	0.36	0.41	0.37	0.26	0.31	0.27	0.40	0.23	0.39	0.33	0.33
	CNN	0.27	0.28	0.51	0.55	0.28	0.23	0.34	0.34	0.44	0.29	0.28	0.34	0.42	0.18	0.36	0.34	0.34

TABLE 5. Scenario 2: Coefficient of variation of relevance scores, across CSI channels and averaged over all CSI samples (CV (channels)), and across CSI samples and averaged over all CSI channels (CV (samples)).

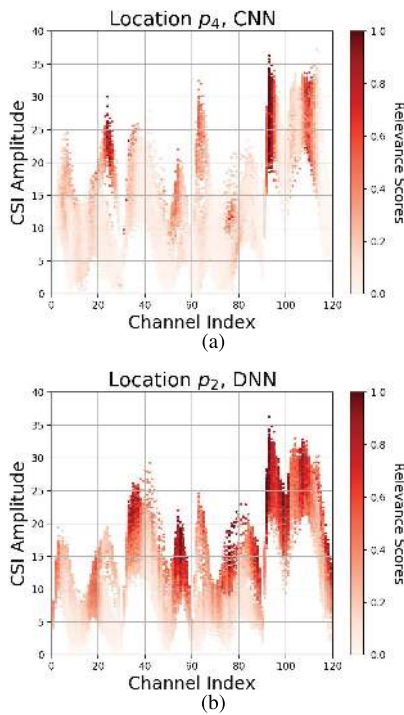| Measure	Scheme	p_1	p_2	p_3	p_4	p_5	p_6	p_7	p_8	p_9	p_{10}	p_{11}	p_{12}	p_{13}	p_{14}	Avg.
CV (channels)	DNN	0.64	0.75	0.77	0.69	0.70	0.83	0.75	0.59	0.68	0.8	0.59	0.70	0.76	0.60	0.70
	CNN	1.13	1.26	1.28	1.37	1.57	1.25	1.61	1.31	1.37	1.53	0.97	1.51	1.09	1.33	1.33
CV (samples)	DNN	0.21	0.49	0.39	0.32	0.17	0.44	0.39	0.22	0.29	0.22	0.21	0.36	0.19	0.25	0.30
	CNN	0.54	0.58	1.03	0.84	0.35	0.69	0.35	0.55	0.37	0.38	0.55	0.72	0.41	0.60	0.57

FIGURE 8. Scenario 2: Heatmaps of relevance scores $R'_i, i = 1, \ldots, 120$ superimposed on all testing samples predicted as (a) location p_4 for CNN and (b) location p_2 for DNN. The location corresponding to the worst precision performance for each model (0.23 for CNN and 0.30 for DNN) is chosen.
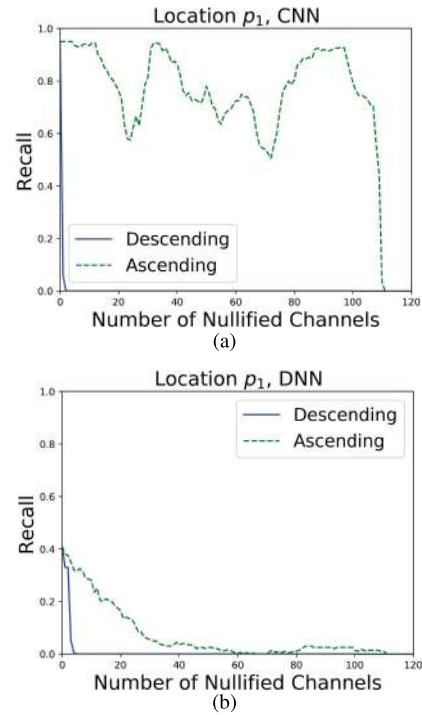

FIGURE 9. Scenario 1: Change in the recall performance after progressive channel nullification, in the ascending or descending order of the relevance scores, on the correctly classified CSI samples of location p_1, for (a) CNN and (b) DNN. CNN outperforms DNN by the largest margin in the recall performance for this location (0.95 for CNN and 0.41 for DNN).

This suggests that CNN can focus on a small subset of relevant, discriminative features for better classification performance (analogous to identifying clearer outlines of an object in image object classification). Quantitatively, by calculating the coefficient of variation (CV), defined as the ratio of the standard deviation to the mean of relevance scores, across CSI channels and averaged over all CSI samples, as summarized in Table 4 and Table 5 as *CV (channels)*, it is seen that CNN yields a higher CV across CSI channels for the locations plotted in Figs. 5–8, as well as all other locations, as compared to DNN.

Consistent patterns across CSI samples contribute to high precision performance. Comparing Fig. 5 and Fig. 6

for Scenario 1, and comparing Fig. 7 and Fig. 8 for Scenario 2, it is observed that the heatmap colors of the testing CSI samples exhibit higher variation and less consistency at the *same* CSI channels when the CNN or DNN model performs poorly (as in Fig. 6 and Fig. 8) than when the CNN or DNN model performs well (as in Fig. 5 and Fig. 7) on respective locations. Specifically, for Scenario 1, visual inspection of Fig. 6 reveals that, among all the testing CSI samples predicted as location p_4 in CNN, some CSI samples exhibit darker red (relevance scores close to one), while other CSI samples exhibit lighter red (relevance scores close to zero), at the same CSI channels 30–35. A similar phenomenon of inconsistent relevance scores across CSI samples is observed for CSI channels
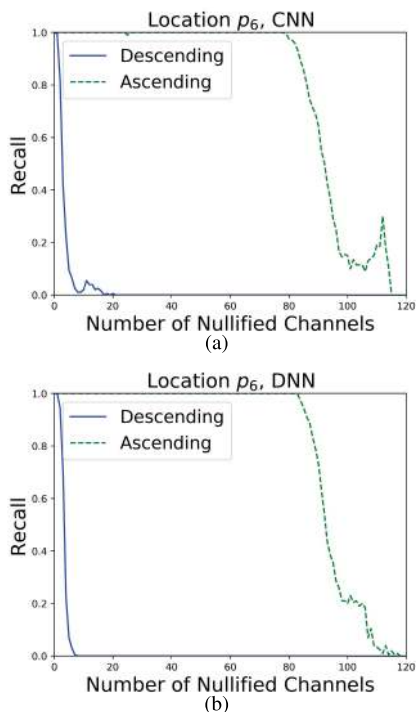
K. M. Chen *et al.*: Interpreting CNNs for Device-Free Wi-Fi Fingerprinting Indoor Localization via Information Visualization

IEEE *Access*

FIGURE 10. Scenario 1: Change in the recall performance after progressive channel nullification, in the ascending or descending order of the relevance scores, on the correctly classified CSI samples of location p_6, for (a) CNN and (b) DNN. Both CNN and DNN achieve the highest recall performance for this location (1.00 for both CNN and DNN).
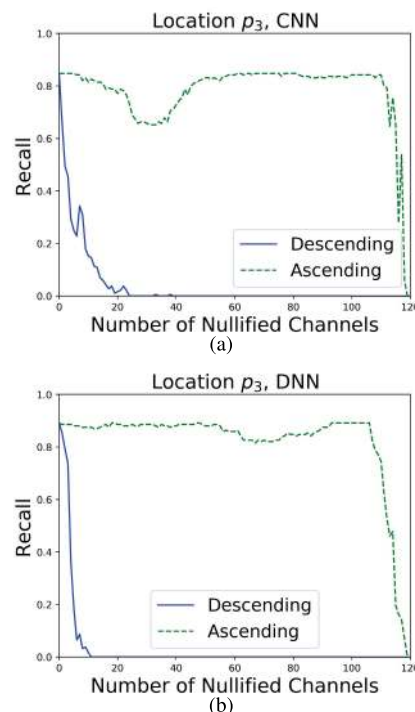

FIGURE 11. Scenario 2: Change in the recall performance after progressive channel nullification, in the ascending or descending order of the relevance scores, on the correctly classified CSI samples of location p_3, for (a) CNN and (b) DNN. Both CNN and DNN achieve the highest or second-highest recall performance for this location (0.85 (second-highest) for CNN and 0.89 (highest) for DNN).

60–70 and 90–100 for location p_3 for DNN. For Scenario 2, a similar phenomenon of inconsistent relevance scores across CSI samples is seen, perhaps even more conspicuously, as the waveforms of CSI samples collectively appear "thicker" due to the more noisy indoor environment. Quantitatively, by calculating the CV across CSI samples and averaged over all CSI channels, as summarized in Table 4 and Table 5 as *CV (samples)*, it is seen that both CNN and DNN models yield smaller CV across CSI samples for high-performing locations than for low-performing locations. Specifically, for the locations plotted in Figs. 5–8, the numbers are: 0.18 for location p_{14} and 0.55 for location p_4 for CNN, and 0.23 for location p_{14} and 0.45 for location p_3 for DNN (Scenario 1); 0.41 for location p_{13} and 0.84 for location p_4 for CNN, and 0.19 for location p_{13} and 0.49 for location p_2 for DNN (Scenario 2). In general, if the patterns are more consistent across CSI samples, which correspond to lower CV across CSI samples, the precision performance is better for a model. This is because if a model learns less clear and explicit pattern about a location, it results in higher misclassification for ambiguous samples and thus lower precision performance.

A small subset of features with the highest relevance scores dominates the model prediction. Fig. 9 shows the effect of progressive channel nullification on CNN and DNN classification for location p_1 in Scenario 1. Location p_1 is where CNN outperforms DNN by the largest margin in the recall performance (0.95 for CNN and 0.41 for DNN). It is

observed that, by performing progressive channel nullification on the CSI samples of location p_1 that are correctly classified, the percentage of correct classification (i.e., recall) decreases. Furthermore, nullifying first the channels with the highest relevance scores ('descending') yields a more rapid decrease than nullifying first the channels with the lowest relevance scores ('ascending'). This shows that a small number of CSI channels with the highest relevance scores are dominant features for model prediction. Similar results are observed for location p_6 in Scenario 1 in Fig. 10, location p_3 in Scenario 2 in Fig. 11, as well as other locations, in our extensive simulations.

The 'ascending' curves exhibit more complicated trends. This can be examined and explained by re-computing the relevance scores after channel nullification progressions. We first examine CNN. For location p_1 in Scenario 1, as shown in Figs. 12(a)–12(c), after 23 runs of 'ascending' channel nullification, dominant features for predicting location p_1 fade (e.g., channels 40–60) and new dominant features not part of the original pattern of location p_1 appear (e.g., channels 5–10). This change of pattern results in the increased model misclassification to other locations and thus the decreased recall (0.58). As the nullification procedure continues, after 34 runs, the influence of channels 5–10 attenuates and the influence of channels 40–60 enhances, thus the increased recall (0.94). For location p_6 in Scenario 1, as shown in Figs. 13(a)–13(c), after 80 runs of 'ascending'
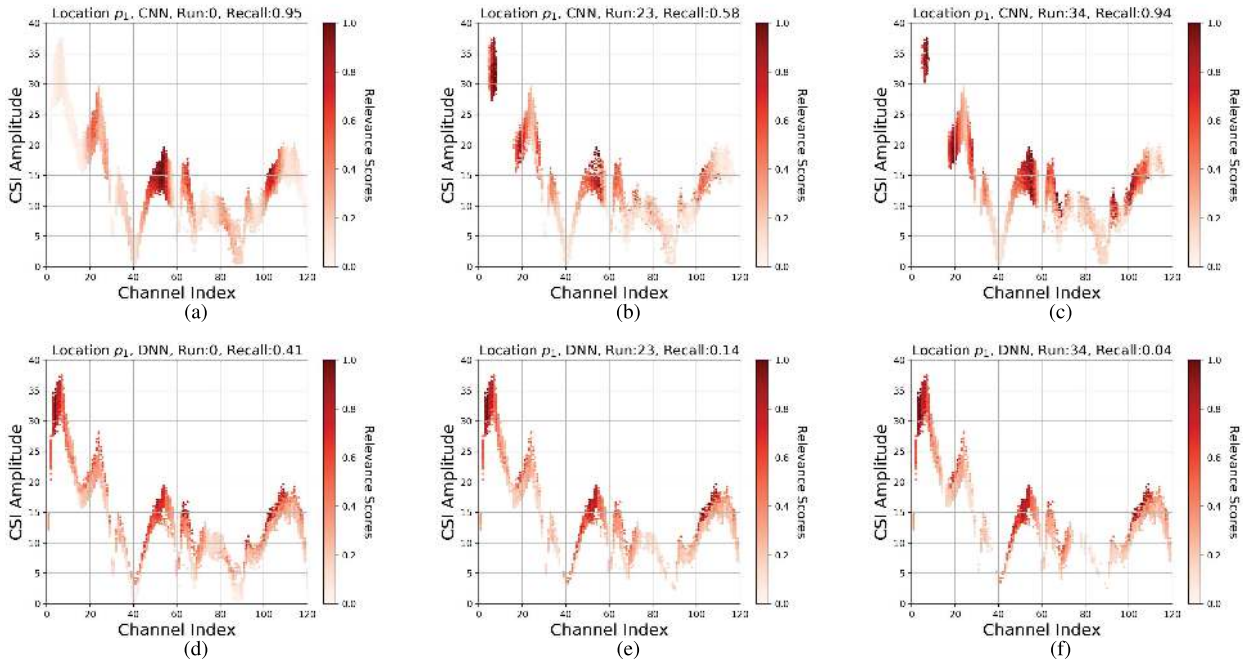
IEEE Access

K. M. Chen *et al.*: Interpreting CNNs for Device-Free Wi-Fi Fingerprinting Indoor Localization via Information Visualization

FIGURE 12. Scenario 1: Heatmaps of relevance scores R'_j, $i = 1, \ldots, 120$ superimposed on the correctly classified CSI samples of location p_1 after 0, 23, and 34 runs of 'ascending' channel nullification, for (a)–(c) CNN and (d)–(f) DNN. (cf. Fig. 9.)
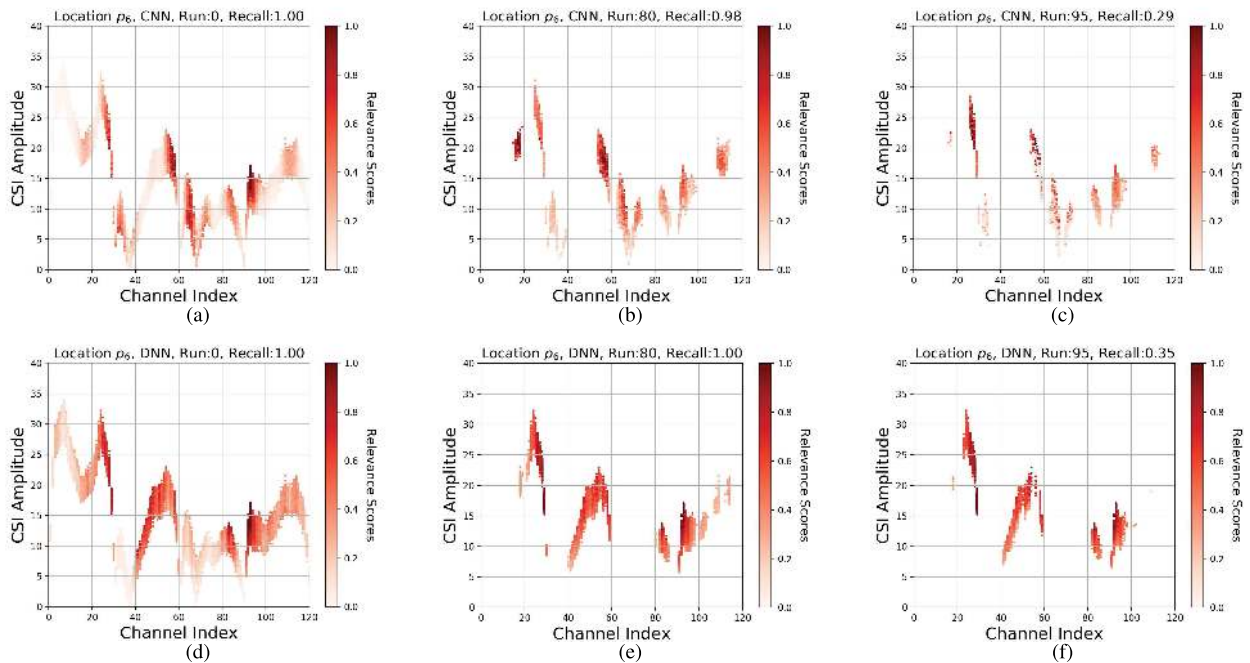

FIGURE 13. Scenario 1: Heatmaps of relevance scores R'_j, $i = 1, \ldots, 120$ superimposed on the correctly classified CSI samples of location p_6 after 0, 80, and 95 runs of 'ascending' channel nullification, for (a)–(c) CNN and (d)–(f) DNN. (cf. Fig. 10.)

channel nullification, dominant features for predicting location p_6 generally remain and no huge dominant features not part of the original pattern of location p_6 appear, and therefore the recall remains almost unchanged (0.98). As the nullification procedure continues, after 95 runs, there is a heightened distortion in CSI, resulting in the decreased recall (0.29).

For location p_3 in Scenario 2, as shown in Figs. 14(a)–14(c), after 30 runs of 'ascending' channel nullification, dominant features for predicting location p_3 fade (e.g., channels 80–90) and new dominant features not part of the original pattern of location p_3 appear (e.g., channels 100–110). This change of pattern results in the increased model misclassification to
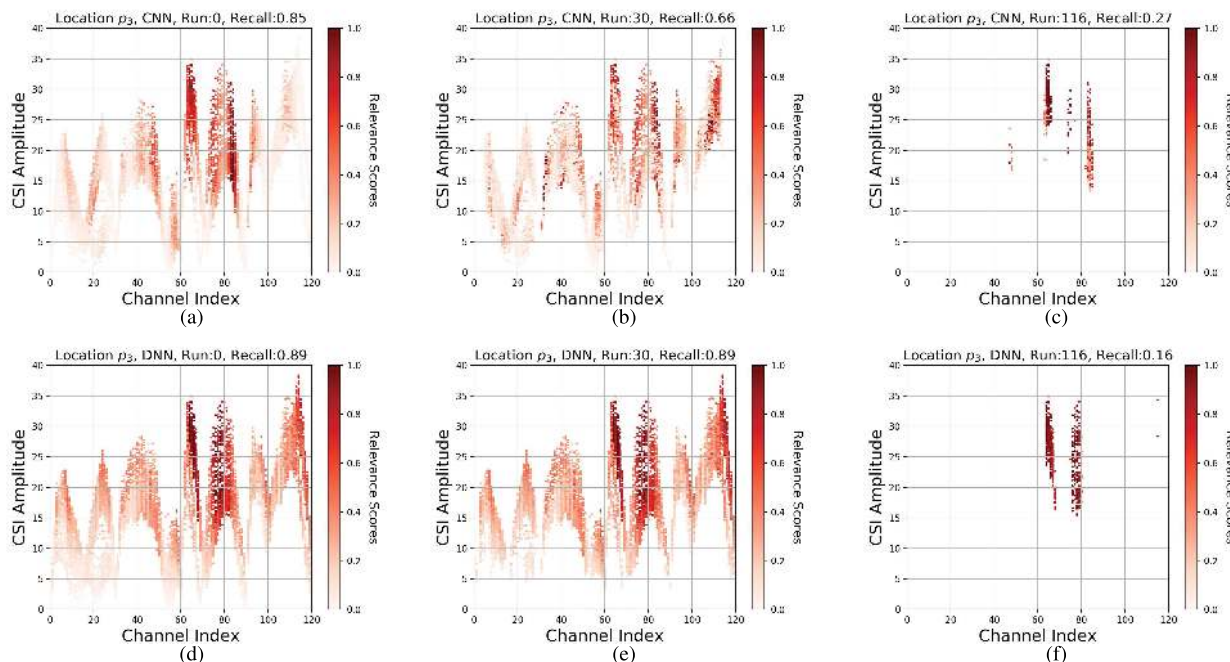
K. M. Chen *et al.*: Interpreting CNNs for Device-Free Wi-Fi Fingerprinting Indoor Localization via Information Visualization

IEEE *Access*

FIGURE 14. Scenario 2: Heatmaps of relevance scores R'_i, $i = 1, \ldots, 120$ superimposed on the correctly classified CSI samples of location p_3 after 0, 30, and 116 runs of 'ascending' channel nullification, for (a)–(c) CNN and (d)–(f) DNN. (cf. Fig. 11.)

other locations and thus the decreased recall (0.66). As the nullification procedure continues, after 116 runs, the heightened distortion in CSI leads to the decreased recall (0.27).

Next, we examine DNN. For location p_1 in Scenario 1, as shown in Figs. 12(d)–12(f),, 'ascending' channel nullification generally results in the attenuation of the original dominant features for predicting the location, and not the generation of new dominant features not part of the original pattern of the location, thus exhibiting a generally decreasing trend in the recall in Fig. 9(b). Different degrees of attenuation, as observed for location p_6 in Scenario 1 in Figs. 13(d)–13(f) and location p_3 in Scenario 2 in Figs. 14(d)–14(f), may lead to different trends and rates of decreasing in the recall. In general, classification results depend on the interplay of various competing factors related to how nullifying channels erases or enhances the evidence for predicting different classes.

VI. CONCLUSION

In this paper, we have modeled the fingerprinting-based indoor localization problem as a classification problem and approached it using a CNN classifier. We showed that the CNN classifier achieves better statistical performance as compared to the k-NN, SVM, and DNN, and has fewer trainable parameters as compared to the DNN. Furthermore, we provided interpretations of CNN and DNN learning over wireless datasets, which cannot be well interpreted by human perceptions. We developed an interpretation framework based on the LRP technique and the CSI channel nullification procedure. The main observations are: 1) clear and explicit location-specific patterns, as learned by the CNN or DNN

model, contribute to high classification performance; 2) consistent location-specific patterns across CSI samples also contribute to high classification performance; and 3) a small subset of features with the highest relevance scores dominates the model prediction.

REFERENCES

[1] D. Macagnano, G. Destino, and G. Abreu, "Indoor positioning: A key enabling technology for IoT applications," in *Proc. IEEE World Forum Internet Things (WF-IoT)*, Mar. 2014, pp. 117–118.

[2] W. Ejaz, M. Naeem, A. Shahid, A. Anpalagan, and M. Jo, "Efficient energy management for the Internet of Things in smart cities," *IEEE Commun. Mag.*, vol. 55, no. 1, pp. 84–91, Jan. 2017.

[3] A. Fotouhi, H. Qiang, M. Ding, M. Hassan, L. G. Giordano, A. Garcia-Rodriguez, and J. Yuan, "Survey on UAV cellular communications: Practical aspects, standardization advancements, regulation, and security challenges," *IEEE Commun. Surveys Tuts.*, to be published.

[4] M. Mozaffari, W. Saad, M. Bennis, Y.-H. Nam, and M. Debbah, "A tutorial on UAVs for wireless networks: Applications, challenges, and open problems," *IEEE Commun. Surveys Tuts.*, vol. 21, no. 3, pp. 2334–2360, 3rd Quart., 2019.

[5] K. Witrisal, P. Meissner, E. Leitinger, Y. Shen, C. Gustafson, F. Tufvesson, K. Haneda, D. Dardari, A. F. Molisch, A. Conti, and M. Z. Win, "High-accuracy localization for assisted living: 5G systems will turn multipath channels from foe to friend," *IEEE Signal Process. Mag.*, vol. 33, no. 2, pp. 59–70, Mar. 2016.

[6] X. Wang, S. Mao, and M. X. Gong, "An overview of 3GPP cellular vehicle-to-everything standards," *GetMobile, Mobile Comput. Commun.*, vol. 21, no. 3, pp. 19–25, Nov. 2017.

[7] H. Seo, K.-D. Lee, S. Yasukawa, Y. Peng, and P. Sartori, "LTE evolution for vehicle-to-everything services," *IEEE Commun. Mag.*, vol. 54, no. 6, pp. 22–28, Jun. 2016.

[8] S.-A. Lazar and C.-E. Stefan, "Future vehicular networks: What control technologies?" in *Proc. Int. Conf. Commun. (COMM)*, Jun. 2016, pp. 337–340.

[9] Z. Yang, Z. Zhou, and Y. Liu, "From RSSI to CSI: Indoor localization via channel response," *ACM Comput. Surv.*, vol. 46, no. 2, pp. 25-1–25-32, Dec. 2013.

[10] J. Xiao, Z. Zhou, Y. Yi, and L. M. Ni, "A survey on wireless indoor localization from the device perspective," *ACM Comput. Surv.*, vol. 49, no. 2, pp. 25-1–25-31, Oct. 2016.

[11] X. Wang, L. Gao, S. Mao, and S. Pandey, "CSI-based fingerprinting for indoor localization: A deep learning approach," *IEEE Trans. Veh. Technol.*, vol. 66, no. 1, pp. 763–776, Jan. 2017.

[12] S. BelMannoubi and H. Touati, "Deep neural networks for indoor localization using WiFi fingerprints," in *Proc. Int. Conf. Mobile, Secure, Program. Netw. (MSPN)*, Apr. 2019, pp. 247–258.

[13] Z. Chen, H. Zou, J. Yang, H. Jiang, and L. Xie, "WiFi fingerprinting indoor localization using local feature-based deep LSTM," *IEEE Syst. J.*, to be published.

[14] R. Y. Chang, S.-J. Liu, and Y.-K. Cheng, "Device-free indoor localization using Wi-Fi channel state information for Internet of Things," in *Proc. IEEE GLOBECOM*, Dec. 2018, pp. 1–7.

[15] X. Wang, X. Wang, and S. Mao, "Deep convolutional neural networks for indoor localization with CSI images," *IEEE Trans. Netw. Sci. Eng.*, to be published.

[16] C.-H. Hsieh, J.-Y. Chen, and B.-H. Nien, "Deep learning-based indoor localization using received signal strength and channel state information," *IEEE Access*, vol. 7, pp. 33256–33267, 2019.

[17] C.-C. J. Kuo, "Understanding convolutional neural networks with a mathematical model," *J. Vis. Commun. Image Represent.*, vol. 41, pp. 406–413, Nov. 2016.

[18] N. Tishby and N. Zaslavsky, "Deep learning and the information bottleneck principle," in *Proc. IEEE Inf. Theory Workshop*, Apr./May 2015, pp. 1–5.

[19] Q.-S. Zhang and S.-C. Zhu, "Visual interpretability for deep learning: A survey," *Frontiers Inf. Technol. Electron. Eng.*, vol. 19, no. 1, pp. 27–39, Jan. 2018.

[20] M. D. Zeiler and R. Fergus, "Visualizing and understanding convolutional networks," in *Proc. Eur. Conf. Comput. Vis. (ECCV)*, 2014, pp. 818–833.

[21] A. Balu, T. V. Nguyen, A. Kokate, C. Hegde, and S. Sarkar, "A forward-backward approach for visualizing information flow in deep networks," in *Proc. NIPS Symp. Interpretable Mach. Learn.*, Dec. 2017. [Online]. Available: https://arxiv.org/abs/1711.06221

[22] S. Bach, A. Binder, G. Montavon, F. Klauschen, K.-R. Müller, and W. Samek, "On pixel-wise explanations for non-linear classifier decisions by layer-wise relevance propagation," *PLoS ONE*, vol. 10, no. 7, Jan. 2015, Art. no. e0130140.

[23] W. Samek, G. Montavon, A. Binder, S. Lapuschkin, and K.-R. Müller, "Interpreting the predictions of complex ML models by layer-wise relevance propagation," in *Proc. NIPS Workshop Interpretable Mach. Learn. Complex Syst.*, Dec. 2016. [Online]. Available: https://arxiv.org/abs/1611.08191

[24] G. Montavon, S. Lapuschkin, A. Binder, W. Samek, and K.-R. Müller, "Explaining nonlinear classification decisions with deep Taylor decomposition," *Pattern Recognit.*, vol. 65, pp. 211–222, May 2017.

[25] W. Samek, A. Binder, G. Montavon, S. Lapuschkin, and K.-R. Müller, "Evaluating the visualization of what a deep neural network has learned," *IEEE Trans. Neural Netw. Learn. Syst.*, vol. 28, no. 11, pp. 2660–2673, Nov. 2017.

[26] D. Halperin, W. Hu, A. Sheth, and D. Wetherall, "Tool release: Gathering 802.11n traces with channel state information," *ACM SIGCOMM Comput. Commun. Rev.*, vol. 41, no. 1, p. 53, Jan. 2011.

[27] J. Hong and T. Ohtsuki, "Signal eigenvector-based device-free passive localization using array sensor," *IEEE Trans. Veh. Technol.*, vol. 64, no. 4, pp. 1354–1363, Apr. 2015.

[28] Y. Liu, W. Xiong, Z. Zhu, and S. Li, "CSI based high accuracy device free passive localization system," in *Proc. IEEE VTC-Fall*, Aug. 2018, pp. 1–5.

[29] X. Chen, C. Ma, M. Allegue, and X. Liu, "Taming the inconsistency of Wi-Fi fingerprints for device-free passive indoor localization," in *Proc. IEEE INFOCOM*, May 2017, pp. 1–9.

[30] N. Srivastava, G. Hinton, A. Krizhevsky, I. Sutskever, and R. Salakhutdinov, "Dropout: A simple way to prevent neural networks from overfitting," *J. Mach. Learn. Res.*, vol. 15, no. 1, pp. 1929–1958, 2014.

[31] S. Knerr, L. Personnaz, and G. Dreyfus, "Single-layer learning revisited: A stepwise procedure for building and training a neural network," in *Neurocomputing* (NATO ASI Series). Berlin, Germany: Springer, Dec. 1990, pp. 41–50.

[32] D. P. Kingma and J. Ba, "Adam: A method for stochastic optimization," in *Proc. 3rd Int. Conf. Learn. Represent. (ICLR)*, May 2015. [Online]. Available: https://arxiv.org/abs/1412.6980

KEVIN M. CHEN received the B.S. degree from the Department of Photonics, National Cheng Kung University, Tainan, Taiwan, in 2015, and the M.S. degree in electrical engineering from National Taiwan University, Taipei, Taiwan, in 2017. Since 2019, he has been a Research Assistant with the Research Center for Information Technology Innovation, Academia Sinica, Taipei, Taiwan. His research interests include automation for software testing and cloud computing infrastructure, user experience and human–computer interaction, deep learning for wireless signal recognition and the Internet of Things (IoT), as well as the frameworks for interpreting deep neural networks for wireless signals.

RONALD Y. CHANG (M'12) received the B.S. degree in electrical engineering from National Tsing Hua University, Hsinchu, Taiwan, in 2000, the M.S. degree in electronics engineering from National Chiao Tung University, Hsinchu, in 2002, and the Ph.D. degree in electrical engineering from the University of Southern California, Los Angeles, CA, USA, in 2008. From 2002 to 2003, he was with the Industrial Technology Research Institute, Hsinchu. In 2008, he was a Research Intern at the Mitsubishi Electric Research Laboratories, Cambridge, MA, USA. In 2009, he was involved with the NASA Small Business Innovation Research projects. Since 2010, he has been with the Research Center for Information Technology Innovation, Academia Sinica, Taipei, Taiwan, where he is currently an Associate Research Fellow (Associate Professor). He was a Visiting Scholar with the Department of Electrical and Computer Engineering, Virginia Tech, Blacksburg, VA, USA, in July–August 2018. His research interests include wireless communications and networking. He was a recipient of the Best Paper Award from the IEEE Wireless Communications and Networking Conference (WCNC), in 2012, and the Outstanding Young Scholar Award from the Ministry of Science and Technology, Taiwan, in 2015 and 2017, respectively. He was an Exemplary Reviewer of the IEEE COMMUNICATIONS LETTERS, in 2012, the IEEE TRANSACTIONS ON COMMUNICATIONS, in 2015, and the IEEE TRANSACTIONS ON WIRELESS COMMUNICATIONS, in 2017.

SHING-JIUAN LIU received the B.S. degree in electrical engineering from National Chung Hsing University, Taichung, Taiwan, in 2014, and the M.S. degree in photonics technologies from National Tsing Hua University, Hsinchu, Taiwan, in 2016. She is currently pursuing the Ph.D. degree with the Department of Electrical and Computer Engineering, University of California at Davis, Davis, CA, USA. From 2017 to 2019, she was a Research Assistant with the Research Center for Information Technology Innovation, Academia Sinica, Taipei, Taiwan. Her research interests include optical wireless communication systems, signal processing for 5G technologies, and machine learning for wireless networks and the Internet of Things (IoT) applications.